scientific reports

Check for updates

OPEN

3D porous structure of ionic liquid-delaminated Ti_3C_2 MXene nanosheets for enhanced electrochemical sensing of tryptophan in real samples

Seyyed Mehdi Khoshfetrat[1]✉, Mobina Motahari[1] & Samaneh Mirsian[2]

Accurate measurement of tryptophan (Trp) levels is crucial for clinical and research purposes, such as nutritional assessment, disorder diagnosis, condition management, and the study of the role of Trp in disease pathophysiology. Herein, the intercalation of 1-octyl-3-methylimidazolium chloride *[OMIM]$^+$Cl$^-$* ionic liquids (ILs) between the layers of Ti_3C_2 MXenes results in a 3D porous structure with a large active surface area and high interlayer spacing (*d*-spacing). Confined *[OMIM]$^+$* ions enhance the electroactive sites and Trp transfer pathways at the Ti_3C_2 MXene and IL interfaces and improve the electron transfer efficiency for Trp oxidation, improving Ti_3C_2 MXene stability via strong π–π and electrostatic Ti_3C_2 MXene–IL interactions. Under optimal conditions, the sensor demonstrated a broad detection range for Trp, ranging from 0.001 to 240 µM, with a low limit of detection of 0.06 nM (S/*N* = 3). Owing to its exceptional stability, selectivity, and reproducibility, the proposed IL-Ti_3C_2/GCE exhibited significant potential for detecting Trp in real amino acid granules and urine samples.

Keywords Electrochemical, Tryptophan, Ti_3C_2 MXene, Ionic liquid, Delamination

Tryptophan (Trp) is required for serotonin production, energy metabolism, and DNA repair. It can be converted to vitamin B3 and form indole compounds, such as kynurenine and quinolinic acid. The kynurenine pathway diverts Trp from serotonin, associated with immunosuppression and tumor growth[1,2]. Adequate Trp levels are crucial for health; Trp deficiency can cause mood disorders, sleep issues, and impaired immunity[3]. Common analytical techniques, such as high-performance liquid chromatography (HPLC)[4], gas chromatography-mass spectrometry (GC-MS)[5], enzyme-linked immunosorbent assay (ELISA), colorimetric assays[6,7], and amino acid analyzers, are used to measure Trp levels in samples. Despite their sensitivity and selectivity, these methods have drawbacks. HPLC and GC-MS methods are expensive and time-consuming, particularly for complex matrices, and require specialized equipment for sample preparation. Derivatization of Trp for volatile analysis is also laborious. ELISA requires specific antibodies, which can be costly and challenging, and there is a risk of false-positive results due to cross-reactivity with similar compounds. Compared with other methods, colorimetric assays have lower sensitivity and specificity and are more susceptible to interference from additional compounds in the sample. Alternatively, electrochemical techniques are highly selective and cost-effective, making them suitable for various applications and users[8,9]. They can detect Trp without interference from other compounds in the sample, simplifying the detection process and reducing potential interferences[10–13]. The challenge of interference in electrochemical Trp detection has led to the development of several strategies to enhance selectivity. Key approaches include electrode modification, where the electrode surface is coated with materials that selectively interact with Trp, and careful control of electrolyte conditions, such as pH, ionic strength, and composition. Additionally, the differences in redox potential among various species significantly contribute to improving sensitivity in electrochemical systems[13,14]. Among the reported modified electrodes (organic[15–17], inorganic[11,18,19], nanomaterials[20–24], etc.), the use of MXenes in the electrochemical detection of Trp offers several advantages[25–27].

[1]Department of Chemistry, Faculty of Basic Sciences, Ayatollah Boroujerdi University, Boroujerd, Iran. [2]Institute of Microelectronics and Microsensors, Johannes Kelper University Linz, Linz, Austria. ✉email: m.khoshfetrat@gmail.com; sm.khoshfetrat@abru.ac.ir

MXenes are a class of two-dimensional (2D) transition metal carbides, nitrides, and carbonitrides with the general formula $M_{n+1}X_nT_x$, where M represents the transition metal (e.g., titanium, vanadium, chromium, molybdenum), X denotes carbon and/or nitrogen, n is an integer (typically 1, 2, or 3), and Tx represents the surface terminations (e.g., -O, -OH, -F)[28,29]. The unique properties of MXenes, such as their excellent electrical conductivity, tunable surface chemistry, high specific surface area, and catalytic activity, make them promising candidates for the development of advanced electrochemical sensors for the detection of Trp. However, owing to the strong van der Waals and electrostatic interactions between the MXene nanosheets, they naturally tend to restack and form multilayered structures[30,31]. This restacking process can lead to the loss of the unique properties of individual MXene nanosheets, such as high surface area and active site accessibility[32]. Various strategies have been used to address restacking issues and maintain the desirable properties of MXene nanosheets, including introducing spacer molecules[15,33–36], combining them with carbon-based materials[37–39], modifying the surface of MXene nanosheets with functional groups[40], and using nanomaterials[41–44]. Imidazolium-based salts, as a popular class of room-temperature ILs, are promising electrolytes for advancing electrochemical technologies because of their high ionic conductivity, broad solubility range, good biocompatibility, exceptional thermal stability, and significant hydrophilic and hydrogen bonding properties. ILs are suggested as a green alternative to traditional molecular solvents for the intercalation and delamination of multilayer materials without significantly altering their surface chemistry or electronic properties. This helps maintain the unique characteristics of MXenes, such as their high electrical conductivity and electrochemical activity. However, the application of IL-assisted delamination of Ti_3C_2 MXenes is still in the infancy stage[45–49].

In this study, 1-octyl-3-methylimidazolium chloride, $[OMIM]^+Cl^-$, was intercalated into Ti_3C_2 MXene, producing a larger *d*-spacing of delaminated MXene, which translates to a greater specific surface area, excellent structural stability, and significantly improved electrocatalytic performance. The imidazole group binds specifically to Trp owing to its positive charge, electron-deficient nature, and π–π interactions, facilitating selective interactions for electron transfer in Trp oxidation. Compared with exfoliated Ti_3C_2-GCE and bare GCE, IL-delaminated Ti_3C_2 had a superior electrooxidation current and a lower overpotential toward Trp with excellent stability, great repeatability, and a low detection limit. The IL-delaminated Ti_3C_2 electrochemical sensor was successfully used to monitor Trp in amino acid granules and human serum samples (Fig. 1).

Experimental section

Materials, apparatus, and synthesis

Section S1 of the Supporting Information provides details of the materials, reagents, and instruments used.

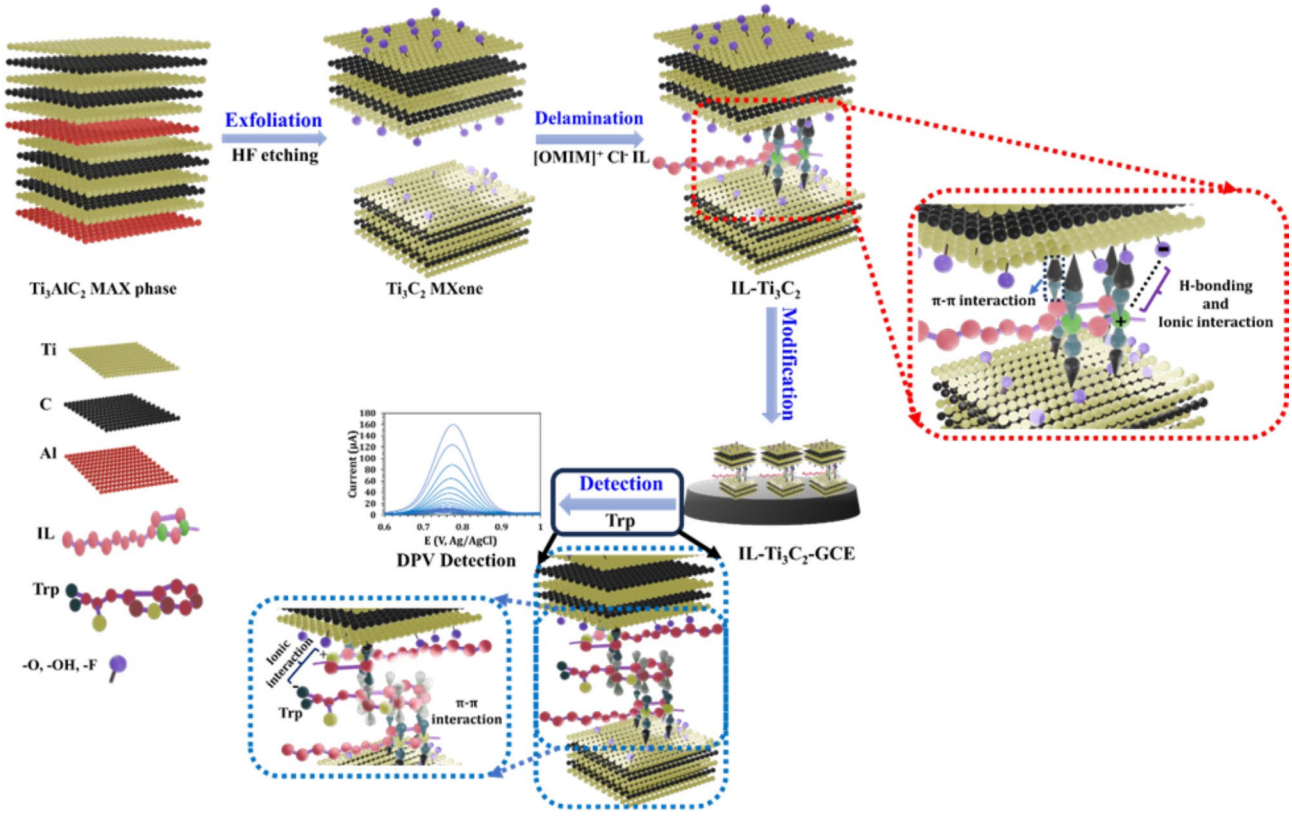

Fig. 1. Schematic preparation of the IL-Ti_3C_2/GCE for enhanced electrochemical sensing of Trp. This Figure was drawn using Blender 4.0, a free and open-source 3D creation software.

Synthesis of the Ti3C2 MXene

Two grams of the Ti_3AlC_2 MAX phase powder were added to 25 mL of concentrated HF (50%) for 18 h of etching. The Ti_3C_2 MXene was then centrifuged with distilled water until the pH of the supernatant was greater than 6. The resulting Ti_3C_2 MXene powder was dried under vacuum for 12 h at 80 °C.

Synthesis pathway for the 1-octyl-3-methylimidazolium chloride ionic liquid [OMIM]+ Cl− IL

To synthesize 0.05 mol (11.53 g) of the ionic liquid 1-octyl-3-methylimidazolium chloride, 0.05 mol (3.98 mL) of 1-methylimidazole was first mixed with 0.06 mol (10.19 mL) of 1-chlorooctane in a single-neck round-bottom flask containing 25 mL of carbon tetrachloride. The mixture was then refluxed for 72 h at 70 °C in an oil bath to ensure that the reaction was complete. Upon completion, a viscous pale-yellow product, $[OMIM]^+Cl^-$, formed at the bottom of the flask, and the solvent was discarded. The final product was washed several times with fresh carbon tetrachloride to remove any impurities. After evaporating the solvent at 80 °C, the highest purity product was obtained, with a yield of 94.0% (10.84 g). The synthesis mechanism is shown in the Supporting Information (Figure S-1).

Preparation of the IL-Ti3C2 flakes

First, the exfoliation of Ti_3C_2 MXene was achieved by ultrasonication of a 1 mg mL^{-1} Ti_3C_2 (1 mL) aqueous solution for 30 min. Subsequently, different amounts of the ILs (0.1 to 1.3 mg) were added to the resulting suspension, and delamination of the Ti_3C_2 MXene was conducted via ultrasonic treatment for 30 min. The planar structure of π-conjugated IL molecules makes them ideal intercalators between the layers of MXenes. This unique configuration enables effective non-covalent π-π interactions, which do not significantly alter the conjugated structure of Ti_3C_2 MXene. Additionally, the electrostatic attraction between positively charged IL molecules and negatively charged MXene layers further promotes IL intercalation. Consequently, the electronic conductivity of the MXene is preserved, ensuring exceptional electrocatalytic activity and high current performance.

Preparation of the electrochemical sensor

The glassy carbon electrode (GCE) was first polished with alumina slurries (0.3 and 0.05 µm) and then cleaned with ethanol and deionized water. Then, 40 µL of the IL-Ti_3C_2 aqueous dispersion was drop-cast onto the cleaned GCE and dried at ambient room temperature to obtain the IL-Ti_3C_2/GCE.

Real sample analysis

Amino acid granules were purchased from a local drugstore. One tablet (containing 500 mg of Trp) was dissolved in 1000 mL of warm distilled water with the aid of ultrasonication for 15 min and then centrifuged at 2000 rpm, after which the supernatant was collected. For the electrooxidation of Trp, 1 mL of the prepared solution was diluted 1000-fold with 0.10 M PB at pH 7.5. The detection of Trp in urine was achieved by diluting healthy volunteers' urine samples with PB (0.1 M, pH = 7.5) at a 1:5 ratio.

Results and discussion

Characterization of the [OMIM]+ Cl− via 1HNMR and FTIR analyses

The HNMR spectrum of the synthesized ionic liquid is presented in the Supporting Information (Figure S-2). The peak at 0.75–1.01 ppm corresponds to the -CH_3 group of the octyl chain (H_1), whereas the region from 1.23 to 1.91 ppm is attributed to the -CH_2 groups in the octyl chain (H_2). The peaks observed at 2.33–2.74 ppm are also attributed to the -CH_2 groups in the octyl chain (H_3). The signals at 4.57–4.70 ppm correspond to another -CH_2 group in the octyl chain attached to the -N in the imidazolium ring (H_4), and the region from 5.05 to 5.48 ppm is associated with the -CH_3 group substituent on the ring (H_5). Finally, the peaks at 7.57–8.19 ppm correspond to the =CH group in the imidazolium ring (H_6). The FTIR spectrum of $[OMIM]^+Cl^-$ (Figure S-3) reveals the bending vibration of the =C-H bond at 804 cm^{-1}, which is linked to the imidazolium ring. The stretching vibration of the C-N bond in the imidazolium ring was observed at 1286 cm^{-1}. The peaks in the range of 1373–1451 cm^{-1} are attributed to the stretching vibrations of C–H bonds and the -CH_3 group in methyl imidazole. The bands at 1490 and 1561 cm^{-1} correspond to the C = C bonds in the aromatic imidazolium ring. The stretching vibration of the C = N bond was observed at 1626 cm^{-1}, and the aliphatic C-H bonds in the octyl chain appeared in the range of 2755–3081 cm^{-1}. Additionally, a weak O-H stretching vibration was observed at 3414 cm^{-1}, likely due to the presence of slight moisture in the structure.

Characterization of the prepared nanomaterials

The effective etching and delamination of Ti_3AlC_2 were confirmed via X-ray diffraction (XRD) analysis (Fig. 2A). The diffraction peaks identified at 11.3°, 19.6°, 34.5°, 36.5°, 39.3°, 42.1°, 45.2°, 48.5°, 52.3°, and 61.5° are consistent with the values associated with the hexagonal close-packed structure of pure-phase Ti_3AlC_2 and correspond to JCPDS PDF file card no. 52–0875[50]. A decrease in crystallinity was indicated by broader peaks and lower intensities in the XRD patterns of Ti_3C_2, along with the disappearance of 104 reflections of Ti_3AlC_2, which signifies the removal of Al layers after HF etching. The (002) peak shifted from 9.7° to 8.6°, reflecting an increase in the d-spacing from 0.9 nm to 1.06 nm as a result of etching and the replacement of Al with -F and -OH/=O functional groups. Importantly, the 002 diffraction peak of the IL-Ti_3C_2 sample shifted to lower angles (6.8°). The expanded interlayer spacing relative to that of pristine Ti_3C_2 was calculated to be 1.85 nm. This can be attributed to the intercalation of $[OMIM]^+$ cations in the MXene interlayers during the delamination process. Furthermore, the increase in the surface area and porosity of the IL-Ti_3C_2 was determined through Brunauer–Emmett–Teller (BET) (Fig. 2B) and Barrett–Joyner–Halenda (BJH) analyses (inset of Fig. 2B). The surface area and porosity of IL-Ti_3C_2 were calculated to be 30.68 m^2 g^{-1} and 14.95 nm, respectively, which are greater than those of Ti_3C_2 MXene (7.83 m^2 g^{-1} and 11.8 nm, respectively). In addition, SEM confirmed the larger interlayer spacing of

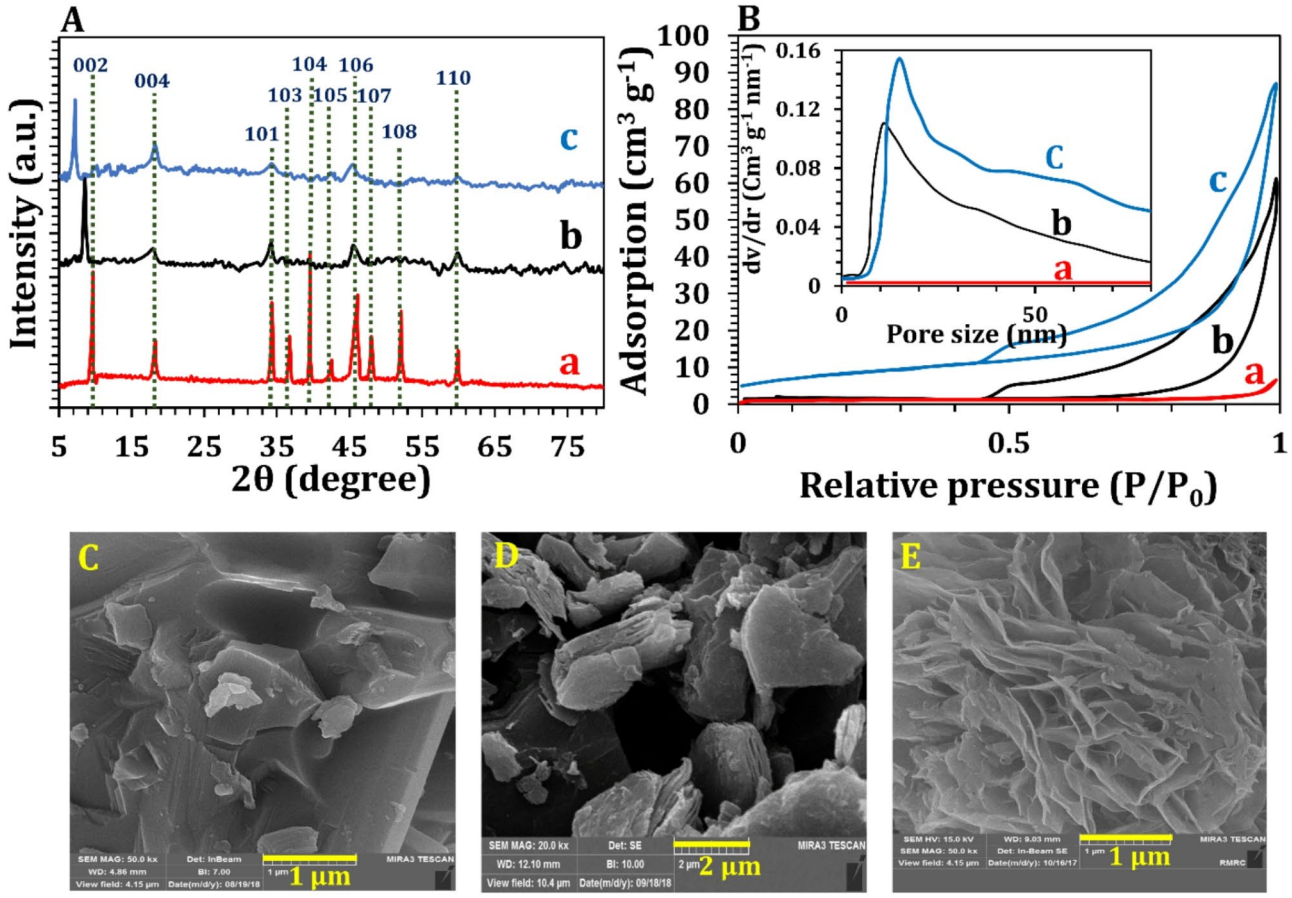

Fig. 2. (**A**) XRD, and (**B**) BET related nanomaterials: (a) Ti_3AlC_2 MAX phase, (b) Ti_3C_2 MXene, and (c) IL-Ti_3C_2. FE-SEM of (**E**) Ti_3AlC_2 MAX phase, (**D**) Ti_3C_2 MXene, and (**E**) IL-Ti_3C_2.

the Ti_3C_2 MXene nanosheets due to the intercalation of *[OMIM]*$^+$ cations, as shown in Fig. 2C to E. Ti_3AlC_2 exhibited a compact and dense structure without exfoliation/delamination before modification (Fig. 2C). Following etching, the resulting Ti_3C_2 MXene exhibited a loosely accordion-like structure with a certain gap between the layers (Fig. 2D). After the IL intercalation, the SEM image of the IL-Ti_3C_2 sample revealed a more open-layered structure of the MXene (Fig. 2E).

Electrocatalytic activity of the IL-Ti3C2/GCE for the oxidation of trp

CV tests were conducted to assess the electrochemical properties of the IL-Ti_3C_2/GCE as an electrocatalytic material for 1 mM Trp oxidation at a scan rate of 100 mV s^{-1} in 0.1 M PB (pH = 7.5). Figure 3A shows the absence of a faradaic current in the voltammograms obtained from the bare GCE (a'), Ti_3C_2/GCE (b'), and IL-Ti_3C_2/GCE (c') in 0.1 M PB (pH = 7.5). The IL-Ti_3C_2/GCE (Fig. 3A, c) catalyst exhibited an extremely high irreversible oxidation peak current response of 86.54 µA for Trp, which is much greater than that of the bare GCE (13.41 µA, Fig. 3A, a) and Ti_3C_2/GCE (27.19 µA, Fig. 3A, b). The increase in the current of the IL-Ti_3C_2/GCE compared with that of the bare GCE (6.4-fold) and Ti_3C_2/GCE (3.2-fold) can be attributed to the greater accessibility of Trp molecules to active MXene sites between layers rather than the outer area of multilayer particles. The intercalation of the IL molecules between the conductive Ti_3C_2 interlayers provided a 3D porous structure with increasing d-spacing from Ti_3C_2 to IL-Ti_3C_2, ensuring adequate exposure of the active species to the Trp and facilitating electron transfer to prevent restacking of the Ti_3C_2 MXenes. Figure S-4 shows that, unlike Ti_3C_2 MXenes, IL-Ti_3C_2 is uniformly dispersed and remains stable in aqueous solution for at least 30 days. The surface roughness, intrinsic activity (synergistic effects), or a combination of the two may be responsible for the increase in activity. The apparent rate constants (K^0_{app}) and C_{dl} for different GCE modifications were compared via the EIS approach (Fig. 3B). In the PB (0.1 M, pH = 7.5) solution containing 1 mM Trp, the rate of electrocatalytic oxidation is represented by K^0_{app}, which is determined via the Eq. (1) $K_{app} = RT/n^2F^2A\,R_{ct}C$[51]. The results showed that the ILs intercalated in between the layer space significantly enhanced the performance of the IL-Ti_3C_2/GCE in comparison to the Ti_3C_2/GCE, resulting in approximately 3.6-fold K^0_{app} and 2.5-fold C_{dl} enhancements (Table S-1). The results indicate that the enhanced activity (69.4%) is mostly attributable to the larger effective surface area of the IL-Ti_3C_2, with synergistic effects accounting for the remaining improvement (30.6%). To determine the Warburg diffusion resistance of Trp molecules in the IL-Ti_3C_2/GCE, the Warburg coefficient (σ) is determined from the slope at low frequencies by graphing Z′ versus $\omega^{-1/2}$ ($\omega = 2\pi f$)[46]. The σ

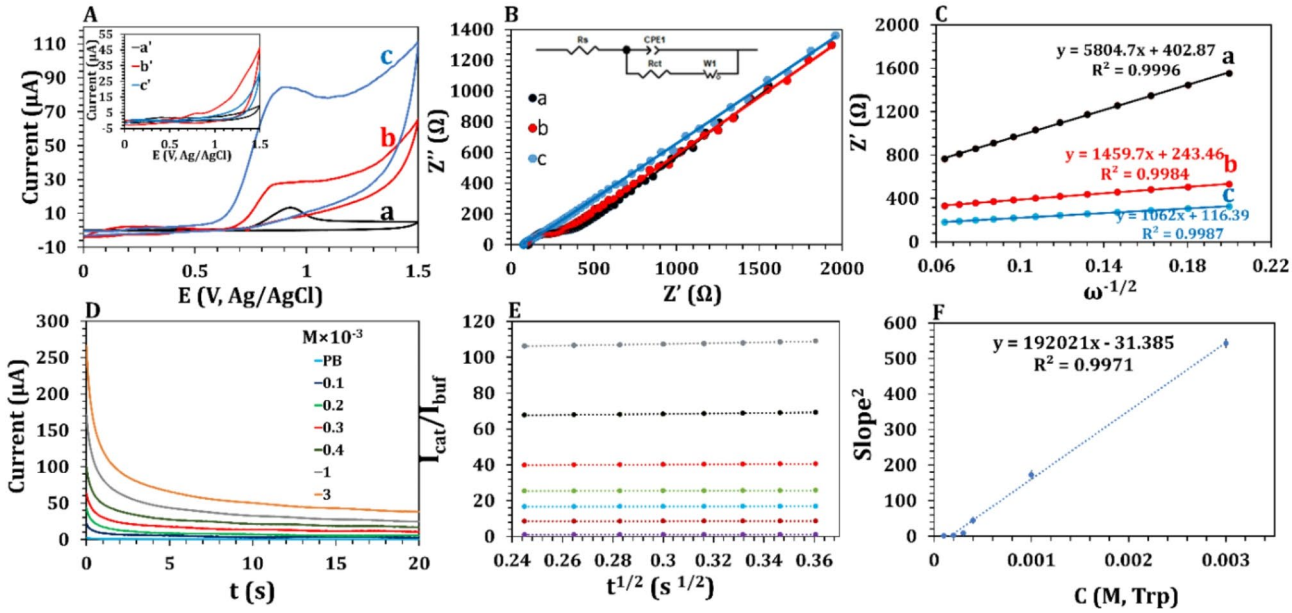

Fig. 3. (**A**) CVs of the different modified GCE in the absence (a′ to c′) and presence of Trp 1 mM (a to c). (**B**) Nyquist plots and (**C**) linearly fitted graph of Z′ against $\omega^{-1/2}$ in the low-frequency region of Nyquist plots in solution PBS (0.1 M, pH = 7.5) + 1 mM Trp, E_{DC} = + 0.9 V. Bare GCE (a′ and a), Ti_3C_2/GCE (b′ and b), and IL-Ti_3C_2/GCE (c and c′). (**D**) Chronoamperograms of IL-Ti_3C_2/GCE in various Trp concentrations. (**E**) and (**F**) depict the plots of I_{cat}/I_{buf} vs. $t^{1/2}$ in various Trp concentrations and square of the slopes in associated (**E**) against the respective concentrations, respectively. Condition: 0.85 V, obtained current at 15 s.

values of the bare GCE (Fig. 3C, a) and Ti_3C_2/GCE (Fig. 3C, b) are 5804.7 and 1459.7 Ω $Hz^{-1/2}$ respectively, whereas the σ of the IL-Ti_3C_2/GCE is 1062 Ω $Hz^{-1/2}$ (Fig. 3C, c). The lower σ of the IL-Ti_3C_2/GCE suggests faster diffusion and Faradic charge-transfer kinetics in the proposed nanomaterial. Moreover, the electrocatalytic activity mechanism was studied via CV by evaluating the electroactive surface areas (ESAs) at various scan rates (20–250) in a 0.1 M KCl solution containing an $[Fe(CN)_6]^{3-/4-}$ (0.5 mM) redox couple (Figure S-5). According to the Randles-Sevcik Eq. (2)[52,53], $I_p = 2.69 \times 10^5 n^{3/2} A D^{1/2} \nu^{1/2} C$, the obtained results indicated a 2.3-fold and 7-fold increase in the ESA of the IL-Ti_3C_2/GCE (0.91 cm^2) (Figure S-5A-B) compared with those of the Ti_3C_2/GCE (0.41 cm^2) (Figure S-5C-D) and GCE (0.13 cm^2) (Figure S-5E-F), respectively. In this equation, A represents the electrode surface area, D represents the diffusion coefficient (7.6×10^{-6} cm^2 s^{-1}), υ represents the scan rate (V s^{-1}), C represents the concentration of $[Fe(CN)_6]^{3-/4-}$ (0.5 mM), and n represents the number of electrons ($n = 1$). The chronocoulometric method was used to further confirm the increase in surface area due to the intercalation of the IL within the MXene layers in the same solution (Figure S-6A). Based on the following Eq. (3), the ESAs obtained from the slope of the plot of Q versus $t^{1/2}$[53] (Figure S-6B) for the bare GCE, Ti_3C_2/GCE, and IL-Ti_3C_2/GCE were 0.11, 0.40, and 0.87 cm^2, respectively, which is consistent with the CV results.

$$Q_{(t)} = \frac{2nFACD^{1/2}t^{1/2}}{\pi^{1/2}} + Q_{dl} + Q_{ads} \tag{3}$$

Interestingly, comparing the ESA and electrooxidation current of Trp (at a scan rate of 100 mV s^{-1}, Fig. 3A) in the IL-Ti_3C_2/GCE and Ti_3C_2/GCE revealed a 3.2-fold increase in the electrocatalytic activity, which was attributed primarily to a 2.2-fold increase (equivalent to 68.75%) in the effective surface area and a 1-fold increase (equivalent to 31.25%) in the synergistic effects, which aligns with the findings from the EIS analysis. Additionally, the improved electrocatalytic capabilities of the IL-Ti_3C_2/GCE in Trp oxidation at a constant potential of 0.85 V were assessed via the chronoamperometric method. The catalytic rate constant (K_{cat})[54] for Trp oxidation using the IL-Ti_3C_2/GCE (6.11×10^4 $M^{-1}s^{-1}$) (Fig. 3D-F) is 4.85 times greater than that of the Ti_3C_2/GCE (1.26×10^4 $M^{-1}s^{-1}$) (Figure S-7). These results demonstrated that the self-assembly of intercalated *[OMIM]*$^+$ ions into 2D Ti_3C_2 MXene nanosheets formed a more open 3D framework with increasing *d*-spacing through spontaneous π–π stacking, electrostatic interactions, and H-bonding. This stable nanomaterial allows for greater access to the active sites of MXenes between layers.

Optimization of various conditions for the electrooxidation of trp

Effect of the amount of IL on sensor performance

By systematically changing the mass ratio of the IL to Ti_3C_2 MXene from 0.1 to 1.3 and measuring the corresponding CV curves, the ideal IL loading was obtained (Figure S-8 A). A progressive increase in response current is clearly observable as the mass ratio of ILs to Ti_3C_2 MXenes increases to 0.9 in 0.1 M PB (pH = 7.5) + 1

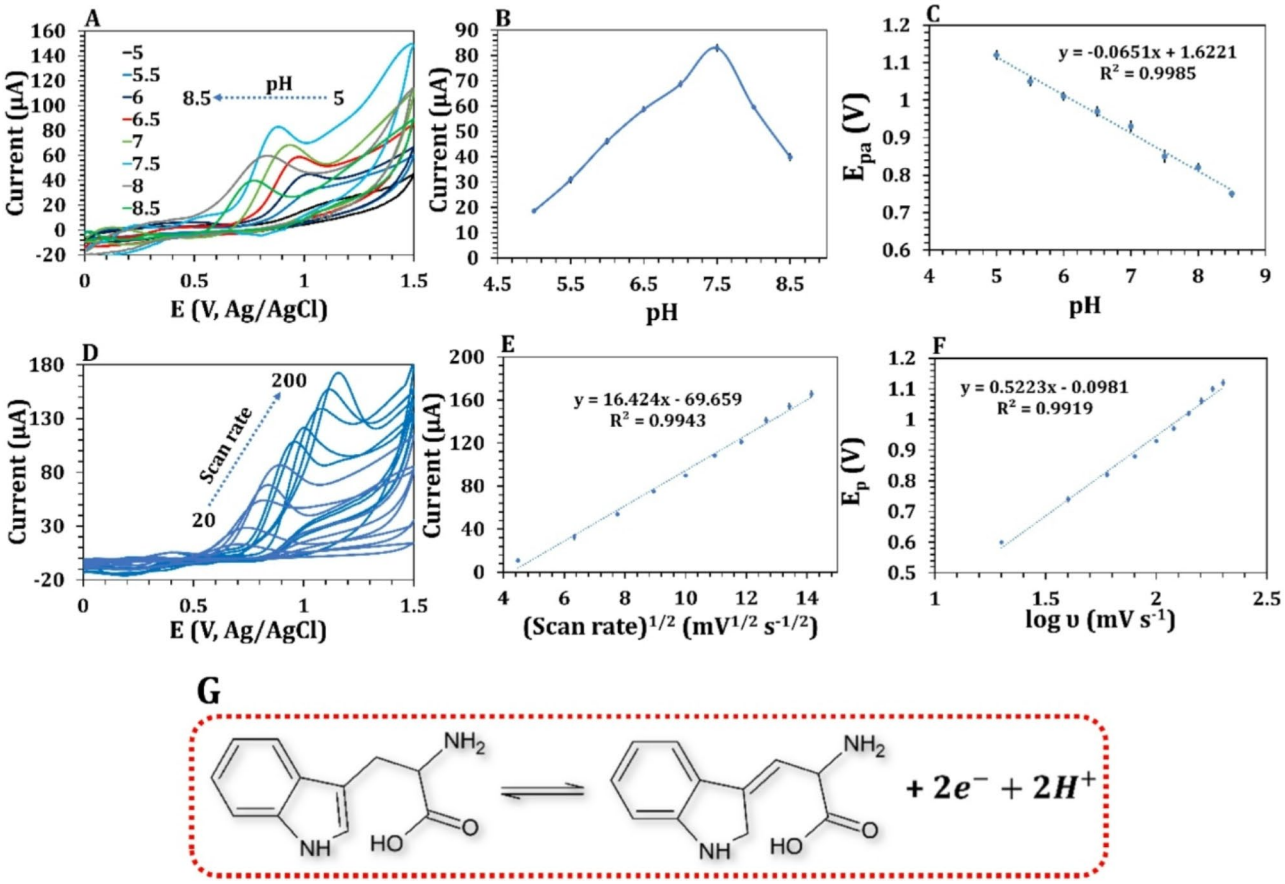

Fig. 4. (**A**) CVs, (**B**) anodic peak current, and (**C**) anodic peak potential of the IL-Ti_3C_2/GCE as a function of pH in solution PBS (0.1 M, pH = 7.5) + 1 mM Trp. (**D**) CVs of 0.1 mM Trp on IL-Ti_3C_2/GCE in PBS (0.1 M, pH = 7.5) at different scan rates (from 20 to 200 mV/s), (**E**) Linear relationship between peak currents vs. square root of scan rate and (**F**) E_p vs. log *v*. (**G**) The suggested electrocatalytic oxidation mechanism of Trp at the IL-Ti_3C_2/GCE.

Sample	Standard (μM)	Average detected	Added	Average Founded	Relative error (%)	SD	RSD (%)	Recovery (%)	$t_{calculated}$	$t_{critical}$
Amino Acid Granules	2.448	2.395 (2.408,2.401,2.43)	0	0	1.606	0.0187	0.077	-	3.639	4.30
			5	7.433 (7.558, 7.389, 7.352)	0.2013	0.1098	1.477	99.79	0.2365	
			10	12.593 (12.28, 12.64, 12.86)	1.167	0.2928	2.325	101.16	0.8597	
			50	51.923 (50.23, 51.89, 53.65)	1.0003	1.710	3.293	98.99	0.5313	
Urine	85.65	83.96 (87.28, 80.36, 84.24)	0	0	1.973	3.468	0.0413	-	0.8439	
			5	91.73 (92.85, 88.64, 93.72)	1.198	2.716	2.961	101.19	0.6927	
			10	96.096 (98.56, 96.45, 93.28)	0.4669	2.657	2.765	100.46	0.2911	
			50	137.91 (140.26, 138.63, 134.84)	1.666	2.780	2.016	101.66	1.407	

Table 1. Electrochemical detection of trp in real-life sample.

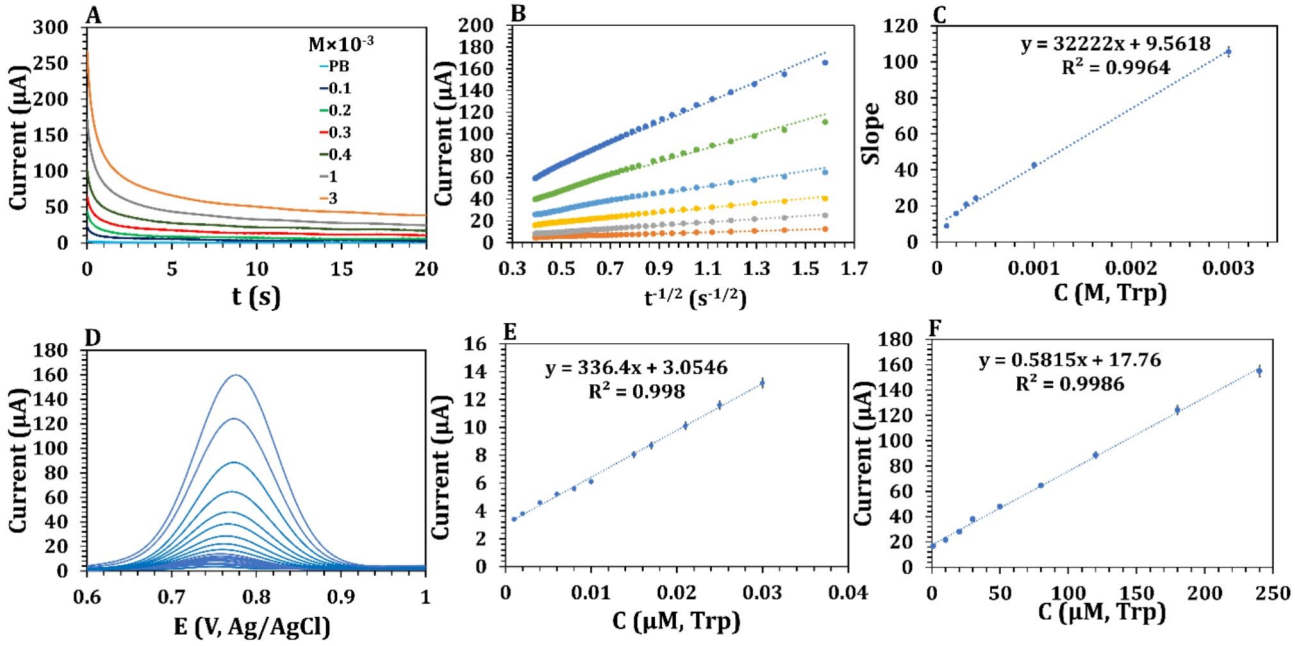

Fig. 5. (**A**) Chronoamperometric obtained at IL-Ti_3C_2/GCE with varying concentrations of Trp. (**B**) (i) plot currents vs. $t^{-1/2}$, and (**C**) plot of the slopes from (**B**) vs. concentration of Trp. (**D**) DPV of IL-Ti_3C_2/GCE in the concentration range of 0.001 to 240 µM in in PBS (0.1 M, pH = 7.5). (**E**) Calibration curve of Trp over the ranges of 0.001 to 0.03 µM and (**F**) 0.03–240 µM ($n = 3$).

mM Trp (Figure S-8B). A further increase in the amount of IL resulted in a lower current due to the instability of the Ti $_3C_2$ MXene sheets and the blockage of the pores of the nanocatalyst.

Effect of the IL-Ti3C2 volume on the determination of trp

Furthermore, we investigated the influence of the IL-Ti_3C_2 volume on the current response (Figure S-8 C). As shown in Figure S-8D, there was a significant increase in the current response with increasing volume from 5 to 40 µL. However, the current response sharply decreased when the volume increased from 40 to 60 µL.

Effect of the IL-Ti_3C_2concentration on trp analysis

The concentration of IL-Ti_3C_2 loaded on the GCE was examined at various dosages in PB (0.1 M, pH = 7.5). As depicted in Figure S-8E, the CV response of the modified GCE exhibited a maximum current at 5.0 mg mL^{-1} (Figure S-8 F), which decreased with increasing concentration. This phenomenon can be attributed to reduced reaction rates resulting from saturation effects where all active sites on the electrode are occupied. In addition, increased concentrations can lead to mass transport limitations that hinder the diffusion of Trp to the electrode. Specifically, increased concentrations of IL-Ti_3C_2 can create a thicker layer that impedes electron transfer between the electrode and the Trp molecules, thereby reducing the sensitivity and response of the system to Trp. In addition, higher concentrations of the ionic liquid can result in a more viscous medium that further restricts the diffusion of tryptophan to the electrode interface and reduces the effective concentration of analyte available for interaction.

Effect of the pH and electrooxidation mechanism of trp

This study examined the impact of the pH of the PB solution on the intensity of the Trp oxidation peak (1 mM). Figure 4A and B show that the electrooxidation response current increases as the pH increases from 5.6 to 7.5 and decreases with increasing pH. Trp has an isoelectric point of 5.89[26], is negatively charged in solution at pH = 7.5, and causes electrostatic attraction between the negatively charged Trp and positively charged IL molecules. In addition, the imidazolium ring structure of the IL on the surface of the nanocatalyst and the Trp molecules are attracted to each other by π–π stacking. Moreover, the functional groups on the Ti_3C_2 MXene can interact with the carboxyl and amino groups on Trp via hydrogen bonding, which enriches them on the electrode surface. Importantly, the anodic peak potential shifted negatively toward a lower potential with increasing pH according to the linear regression equation Ep=-0.0651 pH + 1.6221 ($R^2 = 0.998$) (Fig. 4C). The slope value was close to the theoretical value of -0.059, indicating oxidation behavior with an equal number of electrons and protons. The amount of electron transfer was quantified by conducting coulometric bulk electrolysis experiments. According to the Faraday Eq. (4)[55], $n = {}^{\Delta Q}/_{FCV}$, where $\Delta Q = Q_{Trp} - Q_{PB} = 0.01$ C, $C_{Trp} = 10^{-6}$ M, and V = 50 mL, the electron transfer number was calculated to be 2. The electrochemical Trp oxidation of the IL-Ti_3C_2/GCE in 0.1 M PB at different scan rates (20–200 mV s^{-1}) was investigated (Fig. 4D). The results showed that the process is diffusion-controlled, with a linear plot of the oxidation peak current versus the square root of the scan rate

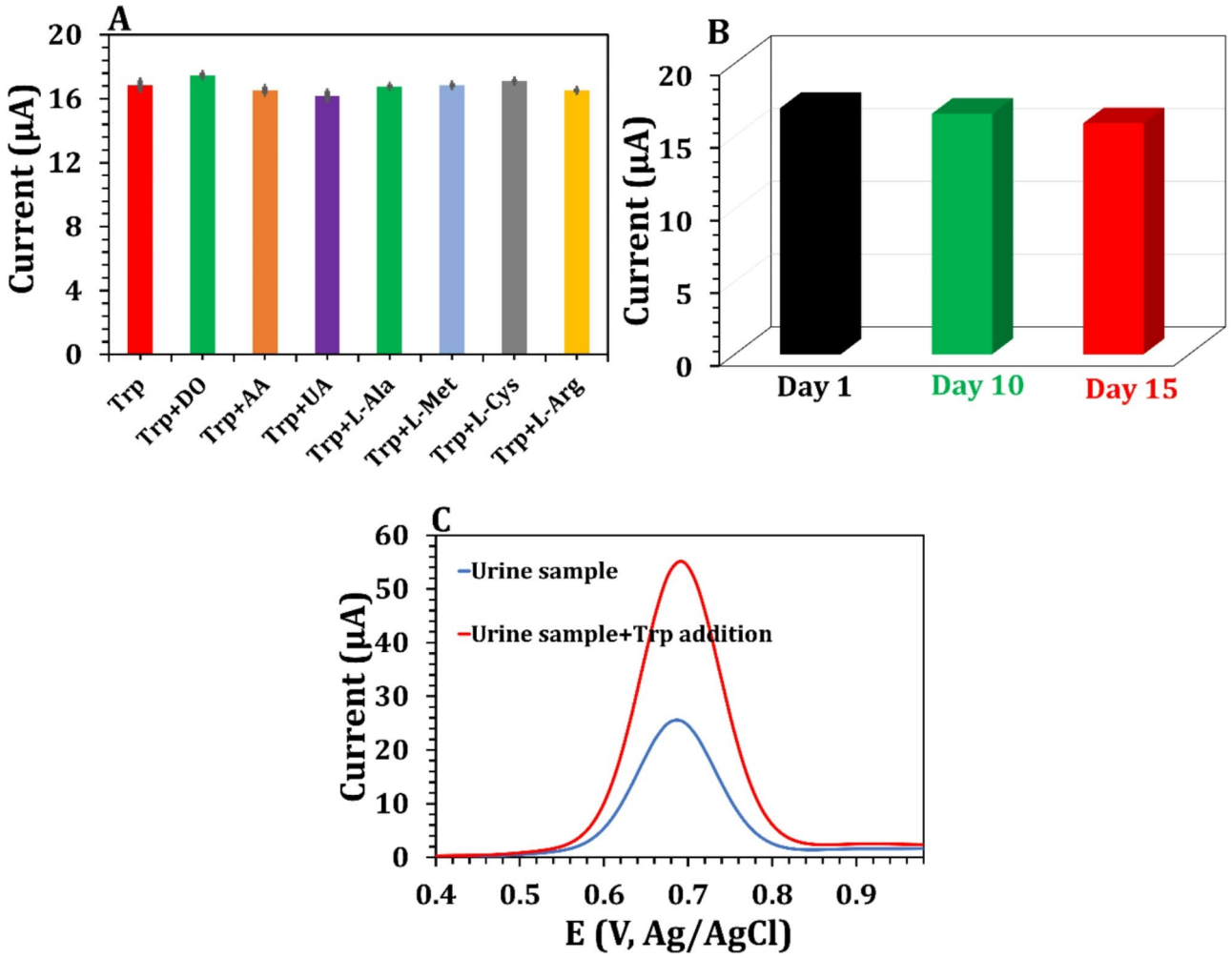

Fig. 6. (**A**) Selectivity of the IL-Ti_3C_2/GCE towards Trp oxidation (1 μM) in the presence of variety of potential interfering compounds (each at 10 μM). (**B**) Stability of the IL-Ti_3C_2/GCE over 15 days. (**C**) DPVs obtained for human urine coupled with spiked Trp (50 μM).

(Fig. 4E). Moreover, the anodic peak currents irreversibly changed toward a higher positive potential as the scan rate increased. The Laviron method (Eq. 5)[56,57] was used to determine the value of (1-α)n, which was determined to be 0.92 based on the slope of Fig. 4F.

$$E_p = E^{0\prime} + \left(\frac{2.303RT}{\alpha\, nF}\right)\log\left(\frac{RTk^0}{\alpha\, nF}\right) + \left(\frac{2.303RT}{(1-\alpha\,)nF}\right)\log\nu \tag{5}$$

The formal potential, heterogeneous rate constant, electron transfer coefficient, and number of electrons are represented by $E^{0\prime}$, k^0, α, and n, respectively. Furthermore, the α value of Trp electrooxidation at the IL-Ti_3C_2/GCE can be calculated via the following Eq. (6)[58].

$$\alpha = \frac{47.7}{E_p - E_{p/2}}\, mV \tag{6}$$

Where $E_{p/2}$ is half of the formal potential value. Consequently, the values of α and the number of electron transfers at the IL-Ti_3C_2/GCE were found to be 0.47 and 2.0, respectively, in agreement with the results of the coulometric analysis. By extrapolating the plot of $E_{p.a.}$ versus the scan rate and calculating $E^{0\prime}$, k^0 was also obtained through the intercept from Laviron's equation. The value of k^0 can be 2.814×10^3 s^{-1}. Overall, the electrooxidation mechanism of Trp at the IL-Ti_3C_2/GCE is shown in Fig. 4G. In addition, the Cottrell equation[59] can be used to determine the diffusion coefficient of Trp, with an estimated value of 1.94×10^{-2} cm^2 s^{-1} (Fig. 5A to C).

Analytical determination of trp on the IL-Ti3C2/GCE

To conduct the concentration study, an IL-delaminated Ti_3C_2/GCE was used to record the current response via DPV. Figure 5D shows the gradual increase in the maximum current as the concentration of Trp increased within the range of 0.001-240 µM, with two linear ranges, 0.001–0.03 µM (Fig. 5E) and 0.03–240 µM (Fig. 5F). The LOD for the IL-Ti_3C_2/GCE was calculated to be 0.06 nM. The considerable decrease in the LOD for Trp may be attributed to a combination of two contributing factors. (i) The increase in surface area with increasing d-spacing from pristine Ti_3C_2 to IL-delaminated Ti_3C_2 makes it more accessible to more active sites of MXenes between the layers. (ii) The π-π interactions between the imidazolium group of the IL and the Trp aromatic ring facilitated charge transfer, thereby enhancing the performance of the sensing platform.

Anti-interference ability, stability, reproducibility, and repeatability

Selectively assessing analytes in a complex physiological environment with interfering species is the main challenge in sensor development. As illustrated by the DPV results (Figure S-9 A and Fig. 6A), interfering substances such as dopamine (DO), ascorbic acid (AA), uric acid (UA), L-alanine (L-Ala), methionine (Met), L-cysteine (L-Cys), and L-arginine (L-Arg) did not affect Trp detection at concentrations 10 times greater (10 µM) than the Trp concentration (1 µM). The shelf life of the biosensor is crucial for practical applications, and the negligible change in DPV current in 1 µM Trp in PB over 15 days (Figure S-9B), with approximately 94% retention of the initial current response (Fig. 6B), demonstrated remarkable stability. In addition, the stability of the IL-Ti_3C_2/GCE was evaluated by conducting 5 consecutive CV tests in a 0.1 M PB solution. The results showed that both the response and the overall shape of the CV curves remained almost unchanged, suggesting that the chemically confined *[OMIM]*$^+$ ions are essential in protecting Ti_3C_2 from oxidation (Figure S-10). To assess the repeatability of the IL-Ti_3C_2/GCE, the oxidation current of one prepared electrode was recorded at 0.01, 1 and 10 μM Trp for three separate measurements across a span of three days (interday) (Table S-2) and within 1 day (intraday) (Table S-3). Overall, the RSD was < 4.5%, with smaller t values for interday and intraday analyses than $|t|_{Critical,2}$=4.30 at $P = 0.05$, indicating no significant systematic errors with good repeatability. For reproducibility, five different independent IL-Ti_3C_2/GCEs were prepared, and their current response was recorded in 0.01, 1, and 100 μM Trp solutions via DPV. The study demonstrated satisfactory reproducibility, with a low RSD ranging from 1.55 to 3.87% ($n = 3$) and smaller t values than $t_{critical,2}$=4.30 (Table S-4). Table S-5 compared previously published electrochemical sensors for Trp to assess the detection capabilities of IL-Ti_3C_2/GCE. The electrochemical sensor demonstrated notable analytical performance that is comparable to and in certain aspects superior to, previously established voltammetric methods for Trp detection.

Application in real samples

To demonstrate the potential applicability of the proposed electrode in the food industry and healthcare, the IL-Ti_3C_2/GCE was applied for the detection of Trp in amino acid granules and human urine (Table 1). The amino acid granule Trp calculated per tablet was 492 mg, which was close to the theoretical value of 500 mg with a 1.6% relative error. Additionally, the recovery test of Trp was performed via the standard addition method by spiking the samples with various concentrations of Trp. The amino acid granule recoveries ranged from 98.99 to 101.16%, with RSD values ranging from 0.077 to 3.3% ($n = 3$). Moreover, the results obtained via the developed sensor showed that this biosensor had excellent accuracy with no systematic error, as evidenced by the small observed |t| compared with $t_{critical,2}$=4.30.

In addition, diluted human serum samples were analyzed to measure Trp. The DPV peak at 0.75 V increased with Trp addition (50 µM), indicating that the oxidation of Trp was detected in the urine samples (Fig. 6C). The recovery values for the urine samples spiked with the Trp standard solution varied from 100.46 to 101.66%, and the RSD values of all three independent tests were less than 3%. These results demonstrate that the developed IL-Ti_3C_2/GCE is highly effective for determining the Trp content in real amino acid granules or urine.

Conclusion

In this study, an increased d-spacing in Ti_3C_2 MXenes was achieved through the intercalation of *[OMIM]*$^+$ IL cations within the MXene layers, resulting in enhanced electrocatalytic performance for the oxidation of Trp. The interface of the IL-Ti_3C_2/GCE exhibited notable stability due to favorable interactions between the MXene and the IL, effectively inhibiting electrode leaching. Consequently, the physically confined *[OMIM]*$^+$ ions increase the availability of electroactive sites, increase electron transfer in surface redox reactions, and improve pathways for Trp molecules. The proposed sensor exhibited successful detection results over a wide range of concentrations, from 0.001 to 240 µM, with a low detection limit of 0.06 nM, indicating strong selectivity and stability. Moreover, the practical efficacy of the IL-Ti_3C_2/GCE was demonstrated by the successful detection of Trp in amino acid granules and human serum samples, which produced satisfactory and validated outcomes.

Data availability

The datasets used and/or analyzed during the current study available from the corresponding author on reasonable request.

Received: 19 November 2024; Accepted: 24 February 2025
Published online: 25 February 2025

References

1. Sinha, A. K. et al. Dietary fibre directs microbial Tryptophan metabolism via metabolic interactions in the gut microbiota. *Nat. Microbiol.***9**, 1964–1978 (2024).

2. Sakurai, M. et al. Serum metabolic profiles of the Tryptophan-Kynurenine pathway in the high risk subjects of major depressive disorder. *Sci. Rep.***10**, 1961 (2020).
3. Kaleta, M. et al. Patients with neurodegenerative proteinopathies exhibit altered Tryptophan metabolism in the serum and cerebrospinal fluid. *ACS Chem. Neurosci.***15**, 582–592 (2024).
4. Desmons, A. et al. High performance liquid chromatography–tandem mass spectrometry quantification of Tryptophan metabolites in human serum and stool – Application to clinical cohorts in inflammatory bowel diseases. *J. Chromatogr. A*. **1685**, 463602 (2022).
5. Kałuzna-Czaplinska, J. & Michalska, M. Rynkowski determination of Tryptophan in urine of autistic and healthy children by gas chromatography/mass spectrometry. *Med. Sci. Monit.***16**, CR488–CR492 (2010).
6. Wang, W. et al. Peptide aptamer-based colorimetric sensor for the detection of L-tryptophan in Porcine serum. *Microchem J.***197**, 109896 (2024).
7. Wu, Y., Wang, T. & Zhang, C. Xing A rapid and specific colorimetric method for free Tryptophan quantification. *Talanta***176**, 604–609 (2018).
8. Momeni, F. & Khoshfetrat, S. M. Zarei electrochemical Sandwich-Type aptasensor based on the multifunctional Catechol-Loaded Au/MIL-53(Fe) for detection of cardiac troponin I. ACS appl. *Nano Mater.***6**, 19239–19248 (2023).
9. Zhang, Y. Wu new perspective crosslinking electrochemistry and other research fields: beyond electrochemical reactors. *Chem. Sci.***15**, 6608–6621 (2024).
10. Tasić, Ž. Z. et al. Electrochemical determination of L-tryptophan in food samples on graphite electrode prepared from waste batteries. *Sci. Rep.***12**, 5469 (2022).
11. Sadok, I., Tyszczuk-Rotko, K. & Mroczka, R. Staniszewska simultaneous voltammetric analysis of Tryptophan and kynurenine in culture medium from human cancer cells. *Talanta***209**, 120574 (2020).
12. Zhang, R. et al. Functionalized PProDOT@ nitrogen-doped carbon Hollow spheres composites for electrochemical sensing of Tryptophan. *Carbon***161**, 842–855 (2020).
13. Nasimi, H. et al. Electrochemical sensors for screening of tyrosine and Tryptophan as biomarkers for diseases: A narrative review. *Microchem J.***190**, 108737 (2023).
14. Khan, Z. A., Hong, P. J. S. & Lee, C. H. Y. Hong recent advances in electrochemical and optical sensors for detecting Tryptophan and melatonin. *Int. J. Nanomed.* **16**, 6861–6888 (2021).
15. Khoshfetrat, S. M. & Mamivand, S. Darband Hollow-like three-dimensional structure of Methyl orange-delaminated Ti3C2 MXene nanocomposite for high-performance electrochemical sensing of Tryptophan. *Microchim. Acta*. **191**, 546 (2024).
16. Xia, H. L. et al. Size-and Emission-Controlled synthesis of Full-Color luminescent Metal-Organic frameworks for Tryptophan detection. *Angew. Chem.***135**, e202308506 (2023).
17. Rezaei, F. & Ashraf, N. Zohuri A smart electrochemical sensor based upon hydrophilic core–shell molecularly imprinted polymer for determination of L-tryptophan. Microchem. *J***185**, 108260 (2023).
18. Mohammadi, F. & Roushani, M. Valipour development of a label-free impedimetric aptasensor based on Zr-MOF and Titaniom carbide nanosheets for detection of L-tryptophan. *Bioelectrochemistry***155**, 108584 (2024).
19. Qian, J. et al. Interfacial superassembly of flower-like NiMn-LDH@poly-l-lysine composites for selective electrochemical sensing of Tryptophan. *Anal. Chim. Acta*. **1237**, 340608 (2023).
20. Liu, Y., Wang, L. & Yang, L. A superior sensor for the electrochemical detection of Tryptophan in food samples using Ag-doped TiO2 nanoparticles modified glassy carbon electrode. *Int. J. Electrochem. Sci.***16**, 210534 (2021).
21. Pan, Q. et al. Development of a chiral electrochemical sensor based on copper–amino acid mercaptide nanorods for enantioselective discrimination of Tryptophan enantiomers. *Anal. Chim. Acta*. **1272**, 341480 (2023).
22. Garg, S., Singh, A. & Parmar, A. S. Rosy Boron carbon Nitride-Assisted Electro-Functionalization of Screen-Printed electrode for Tryptophan sensing. *ACS Appl. Nano Mater.***6**, 14849–14860 (2023).
23. Karimian, M. & Dashtian, K. Zare-Dorabei microfluidic chip and chiroptical gold nanoparticle-based colorimetric sensor for enantioselective detection of L-tryptophan. *Talanta***266**, 125138 (2024).
24. Singh, S. et al. Facile and affordable design of MXene-Co3O4-Based nanocomposites for detection of hydrogen peroxide in Cancer cells: toward portable tool for Cancer management. *Small***19**, 2208209 (2023).
25. Zhang, L. et al. A polyoxometalate/chitosan-Ti3C2Tx MXene nanocomposite constructed by electrostatically mediated strategy for electrochemical detecting L-tryptophan in milk. *Food Chem.* **458**, 140309 (2024).
26. Xue, C. et al. An ionic liquid-modified PEDOT/Ti3C2TX based molecularly imprinted electrochemical sensor for pico-molar sensitive detection of L-Tryptophan in milk. *Food Chem.* **449**, 139114 (2024).
27. Wang, F., Wang, H. & Cui, X. Liu upconversion fluorescence of MXene nanosheets and the sensitive detection of l-tryptophan. *Sens. Diagnostics*. **1**, 1080–1087 (2022).
28. Downes, M., Shuck, C. E., McBride, B. & Busa, J. Y. Gogotsi comprehensive synthesis of Ti3C2Tx from MAX phase to MXene. *Nat. Protoc.* **19**, 1–28 (2024).
29. Amara, U., Hussain, I., Ahmad, M. & Mahmood, K. Zhang 2D MXene-based biosensing: a review. *Small***19**, 2205249 (2023).
30. Khoshfetrat, S. M. Chegeni rational design of Ti3C2 MXene nanocomposite with bromophenol blue for efficient signal amplification: sensitive electrochemical detection of cardiac troponin I in patient plasma. *Sens. Actuators B Chem.***397**, 134668 (2023).
31. Fang, H. et al. Stabilizing Ti3C2T x MXene flakes in air by removing confined water. Proc. Natl. Acad. Sci., 121 e2400084121 (2024).
32. Cao, W. et al. A review of how to improve Ti3C2Tx MXene stability. *Chem. Eng. J.* **496**, 154097 (2024).
33. Naguib, M. et al. Two-dimensional nanocrystals produced by exfoliation of Ti3AlC2, MXenes, Jenny Stanford Publishing2011, pp. 15–29.
34. Ghidiu, M., Lukatskaya, M. R., Zhao, M. Q. & Gogotsi, Y. Barsoum conductive two-dimensional titanium carbide 'clay'with high volumetric capacitance. *Nature***516**, 78–81 (2014).
35. Momeni, F., Khoshfetrat, S. M. & Bagheri, H. Zarei Ti3C2 MXene-based nanozyme as coreaction accelerator for enhancing electrochemiluminescence of glucose biosensing. *Biosens. Bioelectron.***250**, 116078 (2024).
36. Mehdi Khoshfetrat, S., Moradi, M. & Zhaleh, H. Hosseini multifunctional Methyl orange-delaminated Ti3C2 MXene for non-enzymatic/metal-free electrochemical detection of hydrogen peroxide and hydrazine. *Microchem J.***205**, 111382 (2024).
37. Xu, T. et al. Ultralight MXene/carbon nanotube composite aerogel for high-performance flexible supercapacitor. *Adv. Compos. Hybrid. Mater.***6**, 108 (2023).
38. Li, Y. et al. MXene–Graphene Field-Effect transistor sensing of influenza virus and SARS-CoV-2. *ACS Omega*. **6**, 6643–6653 (2021).
39. Zhang, Q. et al. Growth of AgI semiconductors on tailored 3D porous Ti3C2 MXene/graphene oxide aerogel to develop sensitive and selective signal-on photoelectrochemical sensor for H2S determination. *Anal. Chim. Acta*. **1245**, 340845 (2023).
40. Zhang, C. J. et al. Oxidation stability of colloidal two-dimensional titanium carbides (MXenes). *Chem. Mater.***29**, 4848–4856 (2017).
41. Song, X., Gao, H. & Yuan, R. Xiang trimetallic nanoparticle-decorated MXene nanosheets for catalytic electrochemical detection of carcinoembryonic antigen via exo III-aided dual recycling amplifications. *Sens. Actuators B Chem.***359**, 131617 (2022).
42. Huang, J., Gu, H., Feng, X. & Wang, G. Chen copper Nanoparticle/N-Doped Ti3C2Tx MXene hybrids with enhanced Peroxidase-like activity for colorimetric glucose sensing. *ACS Appl. Nano Mater.***5**, 15531–15538 (2022).

43. Liao, L. et al. Fabrication of cobaltous sulfide Nanoparticle-Modified 3D MXene/Carbon foam hybrid aerogels for All-Solid-State supercapacitors. *ACS Appl. Mater. Interfaces*. **13**, 28222–28230 (2021).
44. Wang, B. & Khoshfetrat, S. M. Mohamadimanesh Peroxidase-like manganese oxide nanoflowers-delaminated Ti3C2 MXene for ultrasensitive dual-mode and real-time detection of H2O2 released from cancer cells. *Microchem J.***207**, 111796 (2024).
45. Liang, K. et al. Engineering the interlayer spacing by Pre-Intercalation for high performance supercapacitor MXene electrodes in room temperature ionic liquid. *Adv. Funct. Mater.***31**, 2104007 (2021).
46. Yan, F. et al. A coupled conductor of ionic liquid with Ti3C2 MXene to improve electrochemical properties. *J. Mater. Chem. A*. **9**, 442–452 (2021).
47. Amara, U. et al. Fabrication of ionic liquid stabilized MXene interface for electrochemical dopamine detection. *Mikrochim Acta*. **189**, 64 (2022).
48. Lu, B. et al. Ionic liquid exfoliated Ti3C2Tx MXene nanosheets for photoacoustic imaging and synergistic photothermal/chemotherapy of cancer. *J. Mater. Chem. B*. **10**, 1226–1235 (2022).
49. Jing, M. et al. Ionic liquid etched and microwave-assisted delaminated MXene as an excellent electrocatalyst for the hysteretic negative reaction of vanadium redox flow batteries. *Chem. Eng. J.***455**, 140789 (2023).
50. Chia, H. L. et al. MXene titanium Carbide-based biosensor: strong dependence of exfoliation method on performance. *Anal. Chem.***92**, 2452–2459 (2020).
51. Karimi Shervedani, R. & Torabi, M. Yaghoobi Binder-free prickly nickel nanostructured/reduced graphene oxide composite: A highly efficient electrocatalyst for hydrogen evolution reaction in alkaline solutions. *Electrochim. Acta*. **244**, 230–238 (2017).
52. Suhaimi, N. F., Baharin, S. N. A., Jamion, N. A. & Mohd Zain, Z. Sambasevam Polyaniline-chitosan modified on screen-printed carbon electrode for the electrochemical detection of perfluorooctanoic acid. *Microchem J.***188**, 108502 (2023).
53. Bard, A. J., Faulkner, L. R. & White, H. S. *Electrochemical Methods: Fundamentals and Applications* (Wiley, 2022).
54. Zhang, X., Bao, N. & Luo, X. Ding patchy gold coated Fe3O4 nanospheres with enhanced catalytic activity applied for paper-based bipolar electrode-electrochemiluminescence aptasensors. *Biosens. Bioelectron.***114**, 44–51 (2018).
55. Li, J. et al. A graphene oxide-based electrochemical sensor for sensitive determination of 4-nitrophenol. *J. Hazard. Mater.***201**, 250–259 (2012).
56. Laviron, E. General expression of the linear potential sweep voltammogram in the case of diffusionless electrochemical systems. *J. Electroanal. Chem. Interfacial. Electrochem.***101**, 19–28 (1979).
57. Chen, Y. et al. Facile and fast synthesis of three-dimensional Ce-MOF/Ti3C2TX MXene composite for high performance electrochemical sensing of L-Tryptophan. *J. Solid State Chem.***308**, 122919 (2022).
58. Sangili, A. et al. Highly selective voltammetric sensor for l-Tryptophan using Composite-Modified electrode composed of CuSn(OH)6 microsphere decorated on reduced graphene oxide. *J. Phys. Chem. C*. **124**, 25821–25834 (2020).
59. Manavalan, S., Ganesamurthi, J., Chen, S. M., Veerakumar, P. & Murugan, K. A robust Mn@FeNi-S/graphene oxide nanocomposite as a high-efficiency catalyst for the non-enzymatic electrochemical detection of hydrogen peroxide. *Nanoscale***12**, 5961–5972 (2020).

Acknowledgements

This work was made possible through financial support from the Biosensor and Energy Research Center, Ayatollah Boroujerdi University.

Author contributions

Seyyed Mehdi Khoshfetrat wrote the main manuscript text, prepared the figures and involved in data analysis, computation, finance sources, and validation In addition, S.M.Khoshferat wrote the responses of the reviewers of the article. Mobina Motahari carried out research, assess information, and design tests. Samaneh Mirsian involved in the development of software, editing, and formal analysis of research. Each author evaluates and certifies the work's final report.

Declarations

Competing interests

The authors declare no competing interests.

Additional information

Supplementary Information The online version contains supplementary material available at https://doi.org/10.1038/s41598-025-91773-8.

Correspondence and requests for materials should be addressed to S.M.K.

Reprints and permissions information is available at www.nature.com/reprints.

Publisher's note Springer Nature remains neutral with regard to jurisdictional claims in published maps and institutional affiliations.